Journal of Materials Chemistry

Cite this: *J. Mater. Chem.*, 2011, **21**, 6238

www.rsc.org/materials

PAPER

Access to metastable complex ion conductors *via* mechanosynthesis: preparation, microstructure and conductivity of (Ba,Sr)LiF_3 with inverse perovskite structure†

A. Düvel,[a] S. Wegner,[b] K. Efimov,[a] A. Feldhoff,[a] P. Heitjans[a] and M. Wilkening*[a]

Received 12th October 2010, Accepted 17th February 2011
DOI: 10.1039/c0jm03439h

Highly metastable $Ba_{1-x}Sr_xLiF_3$ ($0 < x \leq x_{max} \approx 0.4$) with an inverse perovskite structure analogous to that of $BaLiF_3$ was synthesized by soft mechanical treatment of BaF_2 and LiF together with SrF_2 at ambient temperature. *Ex* as well as *in situ* X-ray powder diffraction (XRPD) measurements show that heat treatment at 393 K initiates the decomposition of the mixed phase into $BaLiF_3$, LiF and $(Sr,Ba)F_2$. Structural details of the metastable compound (Ba,Sr)LiF_3 were investigated by ultrafast ^{19}F magic angle spinning (MAS) nuclear magnetic resonance (NMR) spectroscopy. Interestingly, five magnetically inequivalent F sites were identified which correspond to fluorine anions coordinated by a variable number of Ba and Sr cations, respectively. Details from XRPD and NMR spectroscopy are discussed with respect to the formation mechanisms and thermal stability of the as prepared fluorides. Impedance spectroscopy is used to characterize (long-range) ionic transport properties. Results are compared with those obtained recently on mechanosynthesized $BaLiF_3$.

I. Introduction

For many years much effort has been spent on developing new ion conductors[1–10] being vital for the successful design of, for instance, high-energy batteries,[8,11–13] fuel cells,[1,2,13] electrochromic devices,[1,2,13] and sensors.[1,2] To at least the same extent, many attempts have been undertaken focussing on the improvement of transport parameters of known ion conductors by, *e.g.* interface engineering.[14–19] In many cases this is done following essentially two routes, *viz* either by (i) varying chemical compositions of, for example, non-stoichiometric compounds or (ii) *via* directed modification of local microstructures in order to take advantage of, *e.g.*, nano-size or interfacial effects while the overall chemical composition roughly remains untouched.[14–18,20–22]

The playground of suitable materials being helpful in the field of interesting ion conductors might be further extended when thermodynamically metastable compounds are made available, see, *e.g.* ref. 23–25. Often, such materials are predicted theoretically,[26–28] however, their synthesis is difficult if not even impossible by employing standard preparation techniques commonly requiring high temperatures. A number of studies exist where metastable compounds have been successfully synthesized by mechanosynthesis (high-energy ball milling) carried out at room temperature by the use of shaker or planetary mills.[29–33] Conspicuously often, the so obtained compounds reveal new structural and electric, as well as magnetic, properties which can be systematically controlled by varying the numerous milling conditions such as the milling time, the kind of vial set used, the ball-to-powder weight ratio, *etc.*[34,35] Therefore, the mechanosynthesis of solids[36,37] is being increasingly considered in the preparation of new functional materials whose properties have to be directed in a specific way.

So far, diffusion properties of metastable crystalline ion conductors prepared by ball milling have been less intensively studied.[23–25,38] In the present paper we will show how mechanosynthesis can be used to prepare a non-equilibrium ion conductor, which is not or only hardly available by high-temperature ceramic synthesis. Structural details are revealed and the formation as well as decomposition mechanisms are studied by both X-ray powder diffraction (XRPD) and ultrafast ^{19}F magic angle spinning (MAS) nuclear magnetic resonance (NMR) spectroscopy. Additionally, the overall ionic conductivity of the highly metastable mechanosynthesized product is investigated by electrical impedance spectroscopy.

The inverse perovskite $BaLiF_3$, see, *e.g.*, ref. 39, can easily be prepared by treating BaF_2 with the same amount of LiF in a high-energy ball mill.[40] Since the product is single phase and of very high purity, it is an ideal model substance to investigate to which degree Sr can be substituted for isovalent Ba in the cubic structure. Here, it turned out that the resulting quaternary fluoride $Ba_{1-x}Sr_xLiF_3$ is very sensitive to heat-treatment.

[a]*Institute of Physical Chemistry and Electrochemistry, and Center for Solid State Chemistry and New Materials (ZFM), Leibniz University Hannover, Callinstr. 3a, D-30167 Hannover, Germany*
[b]*Bruker BioSpin GmbH, Silberstreifen, D-76287 Rheinstetten, Germany. E-mail: wilkening@pci.uni-hannover.de*
† Electronic supplementary information (ESI) available. See DOI: 10.1039/c0jm03439h

At sufficiently high temperature it decomposes leaving over the almost Sr-free $BaLiF_3$ which is much more stable than the quaternary compound. Thus, it is expected that the mixed phase with a large Sr content cannot be prepared by conventional high-temperature solid-state synthesis without taking advantage of, *e.g.*, a well elaborated quenching technique. Even by ball milling carried out below 350 K the upper limit of x reached is approximately 0.3 if $t_{mill} \leq 3$ h. For $t_{mill} > 3$ h larger x values of up to 0.4 are accessible. Let us note that the synthesis of $SrLiF_3$ as well as that of $CaLiF_3$ crystallizing with (distorted) perovskite structure have not been reported in the literature yet.

II. Experimental details

A series of samples with the composition $Ba_{1-x}Sr_xLiF_3$ (Fig. 1) was prepared by joint milling of highly pure BaF_2 (99.99%, Sigma Aldrich), SrF_2 (99.99%, Alfa Aesar), and LiF (99.99%, Alfa Aesar) at ambient temperature. The synthesis was carried out in air using a planetary mill (Fritsch, P7 premium line) operated at a rotational speed of 600 rpm, see also ref. 40. The mill was equipped with a ZrO_2 vial set in combination with 140 milling balls (ZrO_2, 5 mm in diameter). The total mass of each mixture was about 2 g. If not stated otherwise the milling time t_{mill} was set to 3 h. The samples obtained after milling were characterised by X-ray powder diffraction using a Philips PW 1800 as well as a Bruker (D8 Advance) diffractometer both operating with Cu Kα radiation at 40 kV. For transmission electron microscope (TEM) investigations, a powder specimen was dispersed in ethanol, and a drop of 10 μL of suspension was dried on a copper-supported holey carbon film. (Scanning) transmission electron microscopy (S)TEM was made at 200 kV on a field-emission instrument of the type JEOL JEM-2100F-UHR in bright-field, dark-field, and phase contrast.

In order to study the decomposition process of the quaternary fluorides prepared, some *in situ* XRPD measurements (see Fig. S1, ESI†) were carried out using the D8 Advance in combination with a high-temperature cell HTK-1200N (Anton-Paar) flushed with air. Temperatures ranged from 298 K to 973 K. The equilibration time before each scan was 60 min. Heating and cooling rates were set to 12 K min^{-1}.

For the alternating current (ac) conductivity measurements an HP 4192 A analyzer as well as a Novocontrol Concept 80 broadband dielectric spectrometer were employed. The HP impedance analyzer, working at frequencies from 5 Hz to 13 MHz, is connected to a home-built cell with a four-terminal-configuration. The cell is designed such that conductivities can be measured under inert gas atmosphere. Here, the impedance samples were strictly kept under dry nitrogen gas (99.999%). A Eurotherm controller was used to adjust and monitor the temperature (385 K–730 K) near the sample. The Novocontrol impedance spectrometer is equipped with a BDS 1200 sample cell and a BETA analyzer which is capable to measure impedances down to 10^{-14} S at frequencies ranging from a few μHz to 20 MHz. Temperature regulation and controlling within an

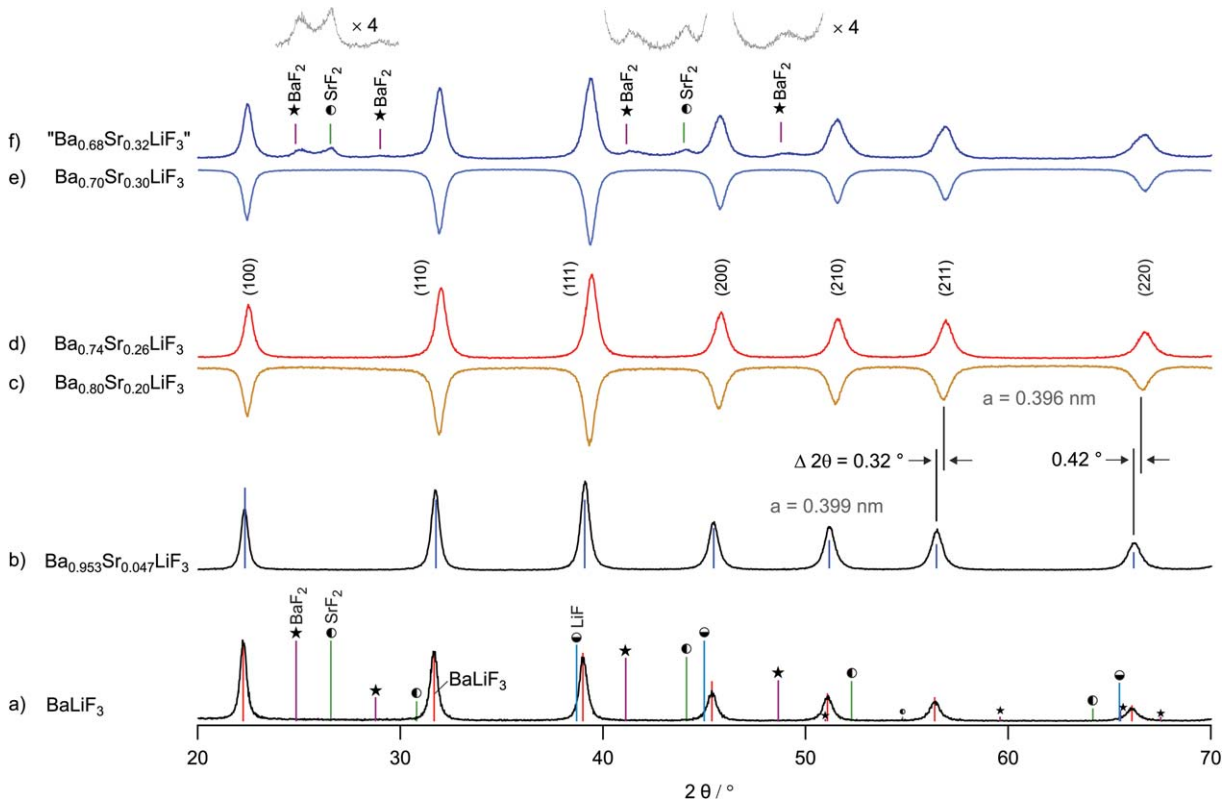

Fig. 1 (a) XRPD of mechanosynthesized $BaLiF_3$ prepared by mechanical treatment of BaF_2 and LiF (molar ratio of 1 : 1) in a planetary mill at 600 rpm (b)–(e) XRPD patterns of $Ba_{1-x}Sr_xLiF_3$ with different compositions x. The peaks slightly shift towards larger diffraction angles (shown for $x = 0.047$ and $x = 0.2$) clearly indicating lattice contraction, *i.e.*, a decrease of a, due to the incorporation of Sr^{2+}. (f) At $x \geq 0.32$ the maximum Sr^{2+} level is exceeded when t_{mill} is set to 3 h. Besides (Ba,Sr)LiF_3 the binary fluorides SrF_2 and BaF_2 show up.

accuracy of about 0.5 K was carried out with a Quattro cryosystem (Novocontrol) using dry nitrogen gas. The root mean square ac voltage was typically 0.1 to 1.0 V. Prior to the measurements the powder samples were uniaxially cold-pressed at 1 GPa to cylindrical pellets which were 8 mm in diameter and approximately 1 mm in thickness. The thickness of each pellet was measured with a vernier calliper. Electrodes were applied either by Au evaporation using an Edwards 306 or by pressing the uncoated pellet between Pt powder. It turned out that the kind of electrodes have no effect on the electrical impedance response measured.

^{19}F MAS NMR spectra were recorded with a Bruker Avance III spectrometer operating at 471 MHz. The NMR spectra were acquired using a single excitation pulse whose length was approximately 2 μs. The spinning speed was $\nu_{rot} = 60$ kHz with room-temperature bearing gas leading to a temperature in the sample chamber of approximately 340 K. Such an ultrafast rotation frequency ensures a sufficiently high resolution of the MAS NMR spectra even in a structurally disordered sample with nm-sized crystallites. Usually, in those materials the ^{19}F MAS NMR line widths exhibit a broader distribution of chemical shifts[23,38,40] than it is observed in their chemically identical but structurally well-ordered counterparts with a much larger mean crystallite size. ^{6}Li MAS NMR spectra of $Ba_{0.74}Sr_{0.26}LiF_3$ were recorded at magnetic fields of 17.6 T and 14.1 T corresponding to the resonance frequencies of 107 MHz and 88 MHz, respectively. The rotation frequency was either 12 kHz (17.6 T) or 30 kHz (14.1 T).

III. Results and discussion

A. Sample characterization by XRD and ^{19}F MAS NMR

1. X-Ray diffraction patterns and TEM micrographs. Mechanical treatment of BaF_2 together with LiF at ambient temperature results in the formation of the inverse perovskite $BaLiF_3$ (space group $Pm\bar{3}m$, $a = 0.3996$ nm, see also ref. 39). In Fig. 1 the corresponding XRPD pattern is shown. Vertical lines indicate the position and intensity of the diffraction peaks which can be found in the literature.[41] Substitution of SrF_2 for BaF_2 leads to the formation of a mixed fluoride while the cubic symmetry of $BaLiF_3$ is retained. Additional diffraction peaks which would indicate the formation of new phases do not show up. With increasing Sr content x the XRPD peaks of $Ba_{1-x}Sr_xLiF_3$ shift towards larger angles 2θ. Thus, the lattice contracts when Ba^{2+} cations (ionic radius of 143 pm)[42] are continuously replaced with the smaller Sr^{2+} ions (127 pm).[42] The mean lattice parameter a can be calculated according to $a = [\lambda/(2\sin\theta)]\sqrt{h^2 + k^2 + l^2}$ where $\lambda = 0.154$ nm is the average wavelength of the Cu Kα radiation used and h, k and l denote Miller's indices of $BaLiF_3$ (see the XRPD pattern of Fig. 1d). In Fig. 2 the parameter a is shown as a function of x. Beginning from $a = 0.3996$ nm ($x = 0$) it decreases to approximately 0.396 nm when the composition reaches $x = 0.3$. The values shown refer to a milling time of 20 h and 10 h, respectively. Similar results are found for shorter milling times if $x < 0.3$. For $t_{mill} = 20$ h the upper composition limit which can be reached by mechanical treatment is about 0.4. For larger values of x the diffraction peaks of SrF_2 and BaF_2 show up in the corresponding XRPD pattern. ^{19}F MAS NMR also revealed the formation of a very small amount of $(Ba,Sr)F_2$ (see below).

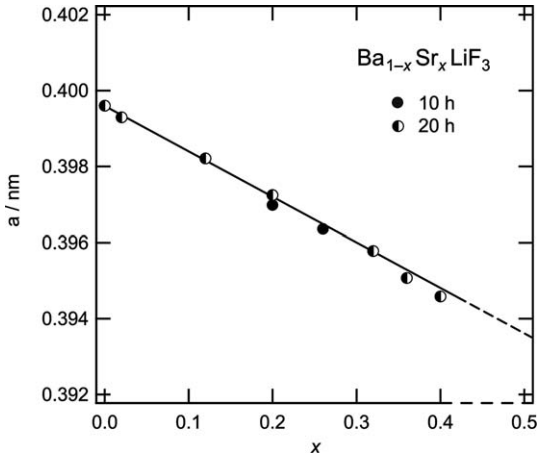

Fig. 2 Lattice constant a of mechanosynthesized $Ba_{1-x}Sr_xLiF_3$ as a function of composition x. The decrease of a indicates the incorporation of the smaller Sr^{2+} ions (ionic radius 127 pm) into $BaLiF_3$. The radius of Ba^{2+} is about 143 pm. See text for further details.

Provided the linear relationship found between a and x (Fig. 2) is valid over the whole composition range, by extrapolating the fit $a(x)$ to $x = 1.0$ the lattice constant of not-yet-synthesized "$SrLiF_3$" can be roughly estimated to $a = 0.3875$ nm. For comparison, the value calculated by Ouenzerfi *et al.*[43] for single crystalline perovskite-type "$SrLiF_3$" is only 0.376 nm.

A rough analysis of the XRPD peak widths $\delta_{2\theta}$ (fwhm, full width at half maximum) of Sr-free $BaLiF_3$ using the formalism introduced by Scherrer[44] (see ref. 23,38 for details of a similar analysis) yields a mean crystallite size $\langle d_c \rangle$ of approximately 25 nm for $t_{mill} = 3$ h. Of course, the Scherrer equation does not consider internal strain ε additionally leading to XRPD peak broadening. Interestingly, with incorporation of Sr, *i.e.*, with increasing x, the peak widths of $Ba_{1-x}Sr_xLiF_3$, which was prepared under the same milling conditions as $BaLiF_3$, increase. This can be clearly seen when the XRPD pattern of a sample with $x = 0.2$ is compared with that of $BaLiF_3$ (Fig. 3). Irrespective of the indices h k l the width $\delta_{2\theta}$ increases by about 37% when going from $x = 0$ to $x = 0.2$. Additionally, we have analyzed the XRPD peaks of a series of samples prepared by milling for 20 h: according to the method by Williamson and Hall[45] which takes peak broadening by strain (see also ref. 23,40) into account, the mean crystallite size $\langle d_c \rangle$ of a sample with $x = 0.26$ turns out to be about 36 nm and ε is of the order of 3.8×10^{-3}. From the corresponding Williamson and Hall plots it is deduced that for this series the crystallite size $\langle d_c \rangle$ decreases from approximately 46 nm at $x = 0.02$ to *ca.* 28 nm when $x = 0.4$ is reached. This increase of the peak width might be either due to a combination of both (i) a smaller mean crystallite size and the additional introduction of internal strain, or (ii) simply due to a larger distribution of diffraction angles in the phase with mixed cations, *i.e.*, due to small variations of a. The first assumption might be explained by the larger hardness of SrF_2, ref. 46, compared to BaF_2, see also ref. 38,23 for a similar comparison. However, our analysis shows that the ε values exhibit a decrease rather than an increase with increasing x. Thus, most likely there is a distribution of lattice

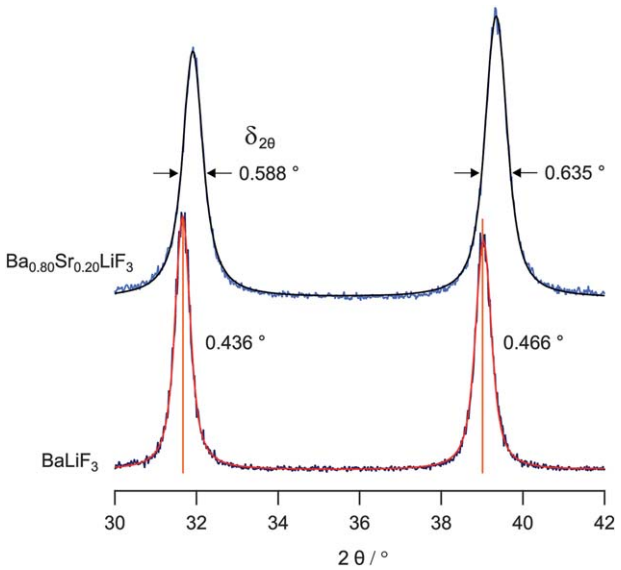

Fig. 3 Magnification of the XRPD patterns of $BaLiF_3$ and $Ba_{0.8}Sr_{0.2}LiF_3$ ($t_{mill} = 3$ h) in the range from $2\theta = 32°$ to 42°. Solid lines represent fits with a combination of Gaussian and Lorentzian lines to obtain the peak widths $\delta_{2\theta}$ indicated.

constants present. This is in agreement with the results from ^{19}F MAS NMR spectroscopy (*vide infra*) revealing a series of different local environments for the F anions. A very similar observation concerning XRPD peak broadening (and ^{19}F MAS NMR) was made for $(Ba,Ca)F_2$ which was also prepared by mechanical treatment of the binary source materials BaF_2 and CaF_2 in a shaker mill, see ref. 23,38.

TEM micrographs roughly confirm the crystallite sizes estimated from XRPD peak broadening. Several micrographs of a sample with the composition $Ba_{0.74}Sr_{0.26}LiF_3$ which was milled for 20 h show crystallites with diameters ranging from 10 to 50 nm. As an example, in Fig. 4 a TEM image of a crystallite is shown characterised by a mean diameter of approximately 45 nm. Defects in the inner regions of the crystallite are difficult to be seen by TEM. While some of the grain boundary regions reveal only a small area fraction showing dislocations being located on the surface of the crystallites (see arrow on the right hand side), there are also regions visible exhibiting structural disorder (see arrows in the lower part of micrograph A in Fig. 4). In these regions, which are characterised by a thickness of only 1 to 2 nm, no long-range order as in the inner part of crystallites is present. However, large amounts of amorphous $(Ba,Sr)LiF_3$, which might additionally influence the transport parameters (see below), are absent. This is similar to mechanosynthesized $BaLiF_3$ investigated by TEM recently.[47]

2. ^{19}F MAS NMR spectra. The ^{19}F MAS NMR spectrum of $Ba_{0.74}Sr_{0.26}LiF_3$ is composed of five signals which can be well resolved using a spinning speed of 60 kHz (Fig. 5). This observation is similar to that made in ref. 48,49. ^{19}F NMR chemical shifts of $Ba_{0.74}Sr_{0.26}LiF_3$, when referenced to C_6F_6, range from 70 to 32 ppm. The NMR line at 70 ppm can be attributed to F anions with four Ba cations as next nearest neighbours ($[Ba]_4$-configuration). For comparison, in $BaLiF_3$ a single NMR line

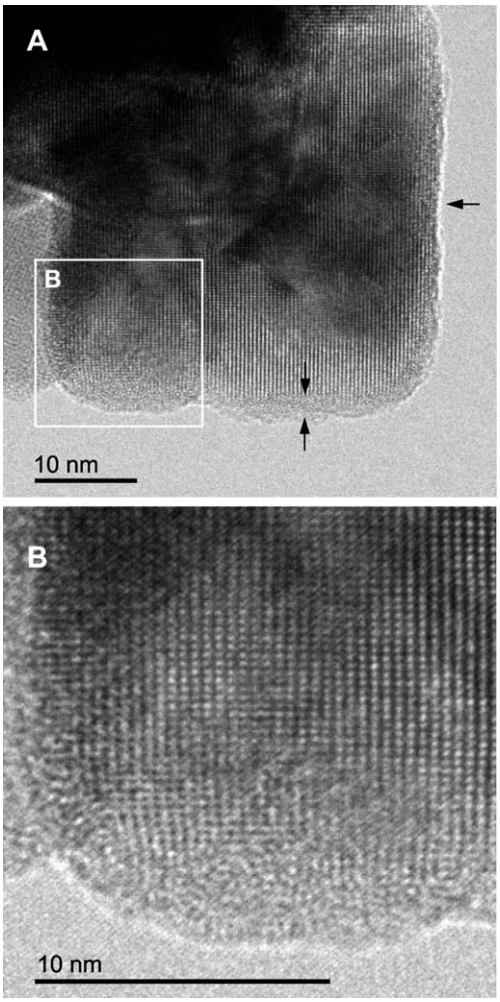

Fig. 4 Typical TEM micrograph of mechanochemically synthesized $Ba_{0.74}Sr_{0.26}LiF_3$ which was treated in a planetary mill for 20 h. The lower image (B) shows the magnification of the rectangular area highlighted in the upper one (A). See text for further discussion.

shows up at 66 ppm. The slight shift towards more positive ppm values might be explained by the lattice contraction observed for $(Ba,Sr)LiF_3$. The fact that in the case of $(Ba,Sr)LiF_3$ no signal is observed at 66 ppm clearly shows that no large amounts of a separate $BaLiF_3$ phase are present. Moreover, neither SrF_2 ($\delta_{iso} = 78$ ppm), BaF_2 (153 ppm) nor LiF (−37 ppm) are detected. Thus, there are no hints pointing to any residual non-reacted source materials. For comparison, the ^6Li MAS spectra, which were recorded at 107 MHz and 88 MHz, respectively, are composed of a single resonance line. The spinning speed was 12 and 30 kHz, respectively.

The successive replacement of Ba with Sr leads to the configurations $[Sr][Ba]_3$, $[Sr]_2[Ba]_2$, $[Sr]_3[Ba]$ and $[Sr]_4$. Analogous structural units were recently found in $(Ca,Sr)F_2$ single crystals with the fluorite structure, *i.e.*, cubic symmetry.[49] According to the assignment of the five ^{19}F NMR lines shown in Fig. 5 the isotropic chemical shift δ_{iso} decreases the more Ba cations are replaced with Sr ions. Thus, the ^{19}F NMR signal of pure "$SrLiF_3$" would show up at δ_{iso} values comparable to that of $[Sr]_4$. The proposed assignment is also reasonable when the

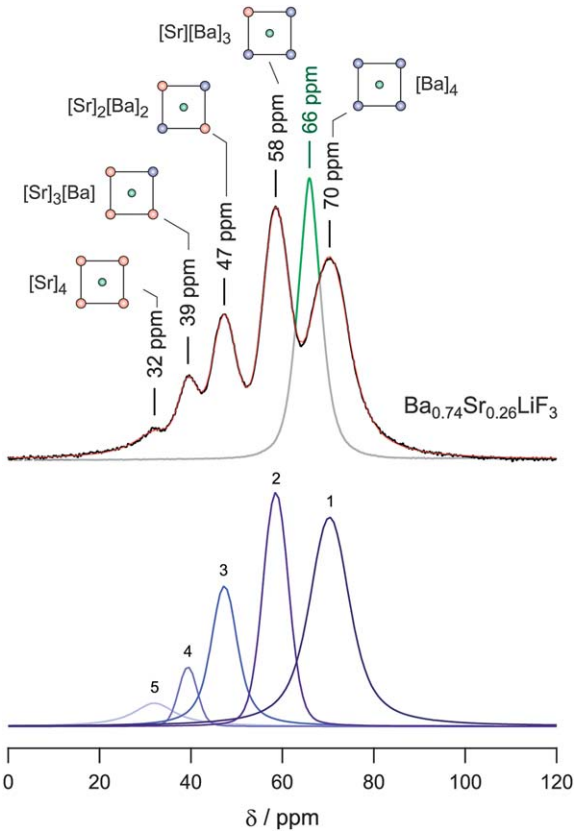

Fig. 5 Solid-state ^{19}F MAS NMR spectrum of mechanosynthesized $Ba_{0.74}Sr_{0.26}LiF_3$ recorded at 471 MHz and a spinning speed of 60 kHz. The spectrum is referenced to C_6F_6. It is composed of five NMR lines with distinct chemical shifts δ_{iso} ranging from 70 to 32 ppm. For comparison, the ^{19}F MAS NMR spectrum of mechanosynthesized $BaLiF_3$ is also shown which consists of a single line at 66 ppm (green line). The red line shows a fit composed of a combination of suitable Voigt functions which are separately shown in the lower part of the figure. Let us note that fitting the spectrum with Gaussian functions leads to a fit of a very similar quality. See text for further details.

NMR intensities and areas under the signals are regarded. Most probably, $[Ba]_4$ as well as $[Sr][Ba]_3$ are formed when the Sr concentration is kept much smaller than that of Ba^{2+} (see also Fig. 6). Indeed, the signals at 70 and 58 ppm dominate the ^{19}F MAS NMR spectrum of Fig. 5. Both the NMR signal at 70 ppm and that located at 32 ppm, which are assigned to $[Ba]_4$ and $[Sr]_4$ units, respectively, show larger intensities as expected for, *e.g.*, a binominal distribution of Ba and Sr on the available lattice sites. Interestingly, the number fraction of Sr-rich units increases with milling time (*vide infra*).

In Fig. 6 the ^{19}F MAS NMR spectra of samples with different compositions are shown which were prepared at a milling time of 20 h. At very small x the spectrum is dominated by the NMR signal of $[Ba]_4$ at 66 ppm. With increasing x the intensity of this resonance decreases and the signal shifts towards $\delta_{iso} = 70$ ppm. Simultaneously, the intensities of the NMR signals attributed to the mixed configurations continuously increase when x values up to 0.3 are regarded. The corresponding area fractions of the different NMR lines are shown in Fig. 7. Of course, the relative populations of the structural units depend on milling time.

The assignment shown in Fig. 5 (as well as in Fig. 6) is also reasonable when the empirical superposition model of Bureau *et al.*[50] developed for ^{19}F NMR isotropic chemical shifts is considered. By using experimental δ_{iso} values of binary fluorides such as LiF, KF, BaF_2, SrF_2 it is possible to estimate isotropic shifts of structurally more complex as well as mixed fluorides in a qualitative manner.[50,51] Here, only the first shell of next nearest neighbours of one fluorine ion is taken into account. The ^{19}F NMR isotropic chemical shift δ_{iso} (with respect to that of C_6F_6) is expressed as the sum of a constant diamagnetic and a paramagnetic term comprising the contributions from neighbouring cations l such as Ba, Sr and Li: $\delta_{iso,calc.} = -127.1\text{ppm} - \sum_l n_l\sigma_l$ where n_l is the coordination number of the fluorine ion and σ_l is given by $\sigma_l = \sigma_{l,0}\exp(-\alpha_l(d - d_0))$. The pre-factor $\sigma_{l,0}$ of the paramagnetic shielding term can be obtained from experimental NMR chemical shifts $\delta_{iso,basic}$ of the so-called basic, *i.e.*, binary, fluorides (*vide supra*) according to $\sigma_{l,0} = -(\delta_{iso,basic} + 127.1\text{ ppm})/n_l$. For BaF_2, SrF_2 and LiF the following $\sigma_{l,0}$ values[50,51] are obtained -70 ppm, -52 ppm and -15 ppm, respectively. While d (*vide supra*) is the distance between the cation and the F anion in the fluoride whose chemical shift has to be calculated, d_0 represents the distance between the cation and the F anion in the related basic fluoride, see ref. 50,51. The (empirical) parameter α_l is given by $\alpha_l = -0.806r_l + 4.048$ where r_l is the ionic radius of the ligand l.[50,51] Here, we used $r_{Li} = 0.078$ nm, and $r_{Ba} = 0.143$ nm.[42] The value of d, which most likely depends on the Ba-Sr-configuration regarded, plays a crucial role in the calculation. In the

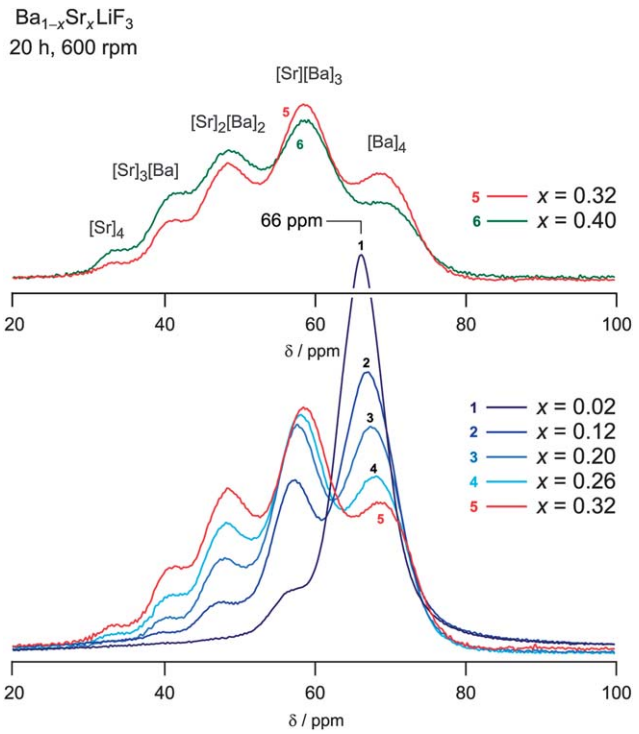

Fig. 6 Solid-state ^{19}F MAS NMR spectra of mechanosynthesized $Ba_{1-x}Sr_xLiF_3$ with different compositions. Data were recorded at 471 MHz and a spinning speed of 60 kHz. The spectra are referenced to C_6F_6. The milling time was set to 20 h; in that case x values of up to 0.4 are accessible. The area fractions of the distinct NMR lines are shown as a function of x in Fig. 7. See text for further details.

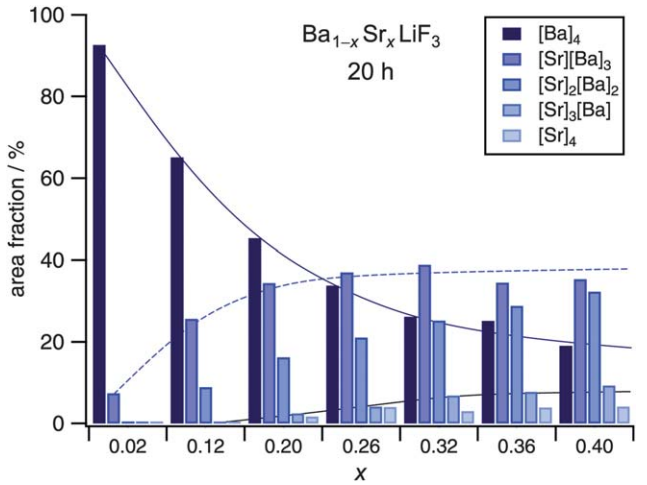

Fig. 7 Area fractions of the distinct ^{19}F NMR lines of $Ba_{1-x}Sr_xLiF_3$ which was prepared by mechanical treatment of the corresponding binary fluorides for 20 h. The lines are to guide the eye. Whereas the number of $[Ba]_4$ units continuously decreases with increasing x, those of the other species, except that of $[Sr][Ba]_3$ possibly passing through a shallow maximum at $x \approx 0.3$ (not indicated), show an increase.

present case we have simply used the lattice constants a of the pure end members $BaLiF_3$ and "$SrLiF_3$" to calculate d (Ba-F) and d (Sr-F). While for $BaLiF_3$ an experimental value can be used; the one calculated by Ouenzerfi *et al.*[43] is taken for "$SrLiF_3$". The Li-F distance is calculated using the mean lattice constant probed for $Ba_{0.74}Sr_{0.26}LiF_3$. Thus, assuming a mean Li-F distance d of 0.198 nm and Ba-F and Sr-F distances of about 0.283 nm and 0.266 nm, respectively, the results shown in Table 1 are obtained.

Let us emphasize that the $\delta_{iso,calc.}$ values obtained have to be regarded as a very rough estimate to understand the experimentally obtained ^{19}F NMR chemical shifts in structurally disordered, mixed $(Ba,Sr)LiF_3$. Nevertheless, the estimation clearly reveals that $\delta_{iso,calc.}$ decreases the more Sr cations are located in the direct neighbourhood of the F anion. Within this superposition model small variations of d can have a very large effect on the resulting chemical shifts. For example, using $a = 0.3875$ nm which is the value found after extrapolation of the fit shown in Fig. 2 (*vide supra*) to calculate d(Sr-F) = 0.274 nm, the following ppm values are obtained: 91, 71, 51, 31, and 10 ppm, respectively. By estimating the specific d values directly from the ionic radii of Ba, Sr and F (0.133 nm), the resulting $\delta_{iso,calc.}$ are very similar to those shown in Table 1. Quite recently, δ_{iso} of pure $BaLiF_3$ was precisely calculated on the basis of DFT calculations.[52] The theoretically predicted value of 68.9 ppm obtained by using a periodic structure model[52] is in good agreement with the experimental one found here (66 ppm) which is identical to that probed by Bureau *et al.*[50] For comparison, the value calculated for $BaLiF_3$ using the empirical superposition model turned out to be 91 ppm indicating the uncertainty of the estimated values.

Table 1 Experimental (±2 ppm) and estimated ^{19}F NMR isotropic chemical shifts of $Ba_{0.74}Sr_{0.26}LiF_3$ by using the empirical superposition model introduced by Bureau *et al.*, see ref. 50

Structural unit	δ_{iso}/ppm	$\delta_{iso,calc.}$/ppm	$\delta_{iso} - \delta_{iso,calc.}$/ppm
$[Ba]_4$	70	92	22
$[Sr][Ba]_3$	58	79	21
$[Sr]_2[Ba]_2$	47	66	19
$[Sr]_3[Ba]$	39	53	14
$[Sr]_4$	32	39	7

Interestingly, a slight shift of δ_{iso} is observed (Fig. 8) when the composition is changed from $x = 0.02$ to $x \geq 0.3$ (Fig. 6), *i. e.*, when a decreases. For example, the signal attributed to $[Sr][Ba]_3$ shifts from about 56.5 ppm at $x = 0.02$ to approximately 59.4 ppm when x reaches a value of 0.4 (Fig. 8). Note that phase-pure samples with x values larger than 0.3 are only obtained when t_{mill} exceeds 3 h. The same trend of δ_{iso} has been recently found for the above mentioned single-crystalline $(Ca,Sr)F_2$ and is discussed in detail in ref. 49.

As mentioned above besides x (see Fig. 6) an increase of t_{mill} also affects the ratio of the line intensities of the NMR spectra shown in Fig. 5 and 6. Investigating this observation in detail one might find out whether any of the five environments are energetically more preferred than others. An attempt is presented in Fig. 9 where the area fractions of the distinct ^{19}F NMR lines of Fig. 5 are plotted as a function of milling time t_{mill}. For comparison, the corresponding spectra of $Ba_{1-x}Sr_xLiF_3$ with $x = 0.26$ are also shown. At the early stages of milling, *i.e.*, at $t_{mill} \approx 30$ min, the most intense signal is that of $BaLiF_3$ being located at 66(1) ppm. With increasing milling time its intensity decreases and δ_{iso} shifts towards 70 ppm. The other NMR signals show a negligible shift with increasing t_{mill}. Thus, besides a small amount of $(Ba,Sr)LiF_3$, the Sr-free inverse perovskite $BaLiF_3$ seems to be the initial product into which Sr is progressively introduced during mechanical treatment (see bottom of Fig. 9).

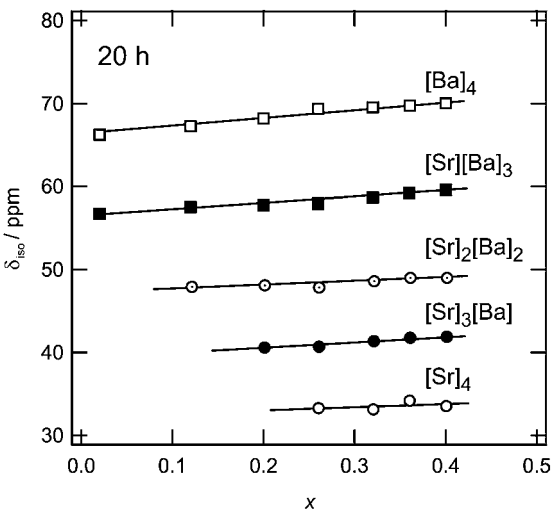

Fig. 8 Variation of the ^{19}F NMR chemical shift of the five distinct F environments in $Ba_{1-x}Sr_xLiF_3$ as a function of composition x. The milling time t_{mill} was 20 h. Note, slightly different results are obtained for $Ba_{0.74}Sr_{0.26}LiF_3$ when t_{mill} is restricted to 3 h (see Fig. 5 for comparison). This indicates that δ_{iso} depends on both composition as well as milling time. The spectra do not show any evidence for residual amounts of the starting materials or the formation of other phases such as $(Ba,Sr)F_2$ (see text for further details).

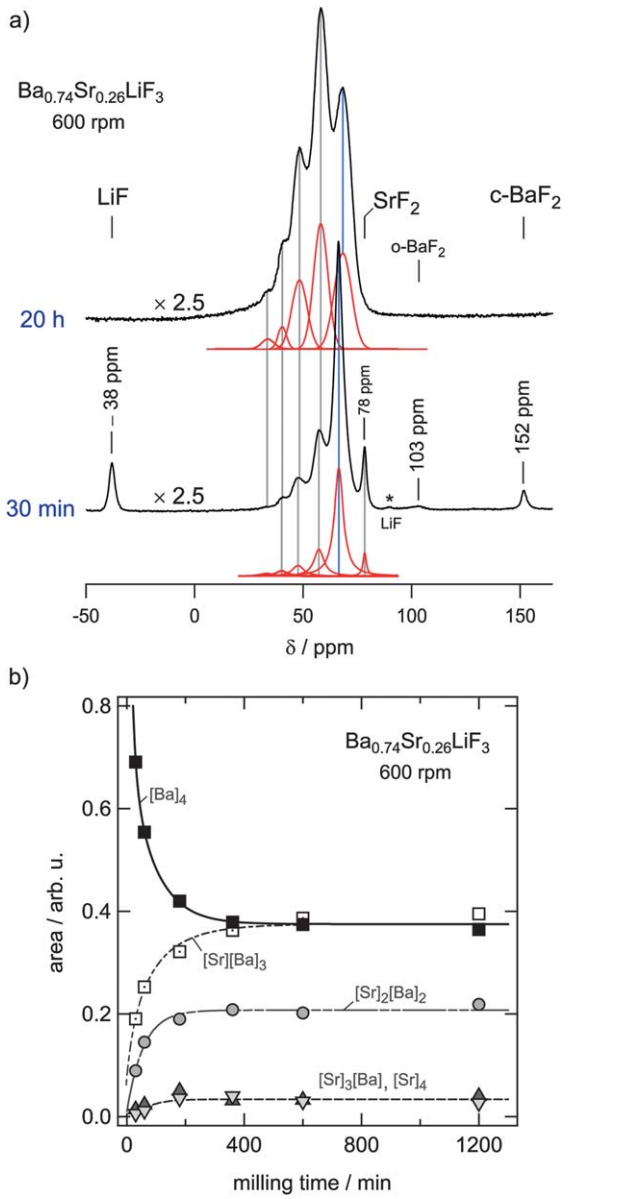

Fig. 9 (a) Solid-state ^{19}F MAS NMR spectra (471 MHz, spinning speed of 60 kHz) of a mixture of cubic-BaF_2, SrF_2, and LiF milled for 30 min and 20 h, respectively, to give (Ba,Sr)LiF_3 of the nominal composition $Ba_{0.74}Sr_{0.26}LiF_3$. (b) Area fraction of the distinct ^{19}F MAS NMR lines of Fig. 5; for comparison, see the ^{19}F MAS NMR spectra displayed in Fig. 9a.

If t_{mill} is chosen to be larger than or equal to 180 min the transformation into (Ba,Sr)LiF_3 is completed and no NMR signals arising from the source materials (LiF, cubic-BaF_2, SrF_2) are detected any more. For t_{mill} larger than 6 h the area fractions of the five NMR lines do not change any longer reaching an equilibrium state.

The NMR signal at 103(1) ppm (Fig. 9a) reveals a small amount of orthorhombic BaF_2, see also ref. 23, being a high-pressure modification of barium fluoride[53–55] whose cubic form was used for mechanosynthesis here. The formation of the orthorhombic form is seen clearest at short milling times. As an example, in Fig. 10a the ^{19}F MAS NMR spectrum of mechanosynthesized $Ba_{1-x}Sr_xLiF_3$ with $x = 0.12$ is presented which gives direct insights into the composition of the reaction mixture at the beginning of the mechanically driven solid-state reaction. In particular, $BaLiF_3$ and orthorhombic BaF_2 can be clearly identified as the initial products formed. In orthorhombic BaF_2 two magnetically inequivalent fluorine positions exist for which two different chemical shift values are expected. These two signals show up at approximately 103 and 174 ppm, respectively (see also ref. 23). To some extent orthorhombic BaF_2 is also produced when cubic BaF_2 is mechanically treated alone or together with LiF to form $BaLiF_3$ (see the ^{19}F MAS NMR spectra of Fig. 10b).

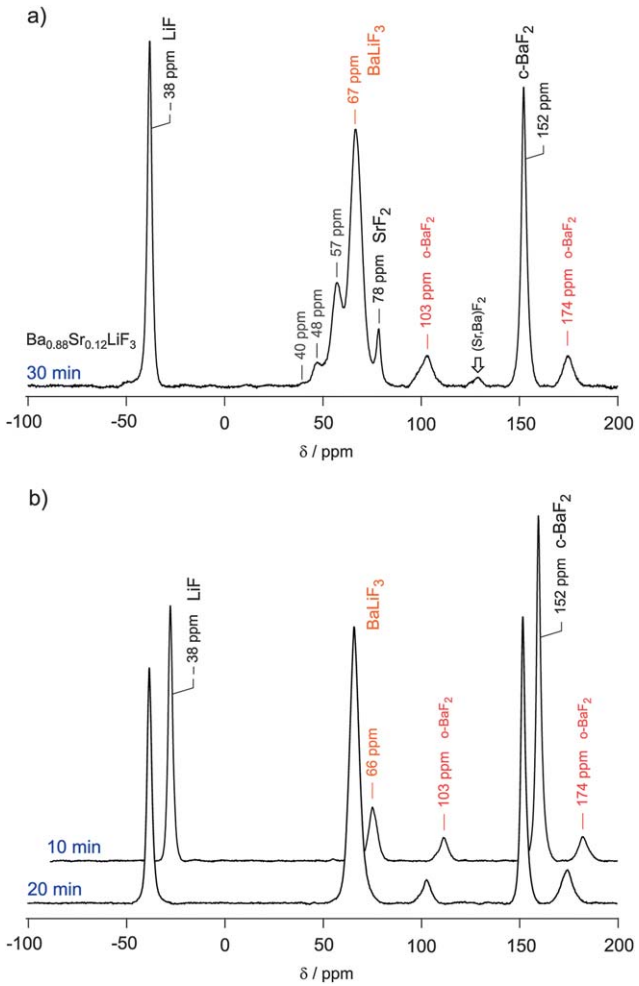

Fig. 10 (a) ^{19}F MAS NMR spectra (471 MHz, 60 kHz spinning speed) of a mixture of cubic BaF_2, SrF_2 and LiF which was mechanically treated for only 30 min to enlighten the early stages of milling. Chemical shift values presented are referenced to C_6F_6. Increasing t_{mill} to 180 min results in phase-pure (Ba,Sr)LiF_3 and the NMR signals of the source materials (LiF: −38(1) ppm, cubic BaF_2: 152(1) ppm, SrF_2: 78(1) ppm) as well as those of orthorhombic BaF_2 (103(1) and 175(1) ppm, respectively) cannot be detected any longer (for comparison, see the NMR spectra presented in Fig. 9). (b) Stacked plot of two ^{19}F MAS NMR spectra of a stoichiometric mixture of LiF and BaF_2 leading to phase-pure $BaLiF_3$ at sufficiently large milling times. NMR spectra were recorded at a resonance frequency of 471 MHz and a spinning speed of 60 kHz. At very short t_{mill} a relatively large amount of orthorhombic BaF_2 is detected which is also seen in the corresponding XRPD patterns.

One might suppose that the intermediate formation of orthorhombic BaF_2 is a necessary pre-step for the successful mechanosynthesis of $BaLiF_3$ which, in the presence of SrF_2, then transforms into (Ba,Sr)LiF_3. Note that the crystallographic structure of orthorhombic BaF_2 resembles the inverse-perovskite structure of $BaLiF_3$. For comparison, by means of high-energy ball milling the synthesis of $SrLiF_3$ and $CaLiF_3$, expected to crystallize with a highly distorted perovskite structure if at all, has not been observed yet. This fact might be due to the circumstance that the corresponding orthorhombic modifications of SrF_2 and CaF_2 as well require much higher pressures to be formed.[53] Even when SrF_2 or CaF_2 are mechanically treated under the milling conditions as described here, there are no indications that the orthorhombic phase is created.

Finally, concerning Fig. 10a, the NMR intensity showing up at approximately 128 ppm (marked by a small arrow) presumably reflects the unresolved ^{19}F MAS NMR lines of a small amount of (Ba,Sr)F_2 (*vide infra*).

B. Decomposition of mechanosynthesized (Ba,Sr)LiF_3 as followed by XRD and ^{19}F MAS NMR

The metastable character of mechanosynthesized, nanocrystalline (Ba,Sr)LiF_3 comes to the fore when the phase-pure product is exposed to elevated temperatures for several hours. As an example, in Fig. 11 the XRPD patterns of $Ba_{0.74}Sr_{0.26}LiF_3$ are shown which was annealed for 3 h at 493 K and 1030 K, respectively. After exposing the sample at 1030 K the Sr-containing inverse perovskite is largely decomposed. In fact, the decomposition process starts already at lower temperatures; annealing $Ba_{0.74}Sr_{0.26}LiF_3$ for 3 h at 393 K leads to the emergence of SrF_2 peaks of very low intensity (see Fig. 11). The XRPD peaks of LiF partly overlap with those of $BaLiF_3$ as well as BaF_2 (Fig. 1) and, thus, are hardly detectable. Interestingly, no oxides are formed during the decomposition process which was carried out in air; this was also verified using *in situ* X-ray diffraction (Fig. S1, ESI†). Much more surprising is the fact that no BaF_2 can be seen after heat treatment. This is also confirmed by an *in situ* XRPD measurement carried out up to 973 K (Fig. S1, ESI†). Thus, $BaLiF_3$, from which SrF_2 as well as LiF are removed, is the main decomposition product.

Interestingly, the 2θ values of the new peaks showing up are slightly shifted towards smaller diffraction angles. Most probably, a very small amount of Ba is incorporated into SrF_2 leading to a mixed (Sr,Ba)F_2 phase. Indeed, mechanical treatment of SrF_2 together with BaF_2, but in the absence of LiF, unequivocally leads to the formation of structurally disordered (Sr,Ba)F_2 (see Fig. 12). The other way round, $SrF_2 + BaF_2 \rightarrow 2(Sr,Ba)F_2$ might be regarded as a competitive reaction with respect to the formation of (Ba,Sr)LiF_3 as well as $BaLiF_3$. The presence of SrF_2 seems to hinder the reaction $BaF_2 + LiF \rightarrow BaLiF_3$ since non-reacted BaF_2 is detected in the XRPD pattern of Fig. 1f when x is chosen to be large enough and t_{mill} set to 3 h. Moreover, increasing x to about 0.5 clearly leads, besides (Ba,Sr)LiF_3, to the formation of (Sr,Ba)F_2 if $t_{mill} > 10$ h. Even when the milling time is increased to 48 h or a vial set of tungsten carbide (WC), having a density (14.95 g cm^{-3}) much larger than that of ZrO_2 (6.06 g cm^{-3}), is used, residual (Sr,Ba)F_2 is detected by XRPD. This also shows that even under these extreme milling conditions large

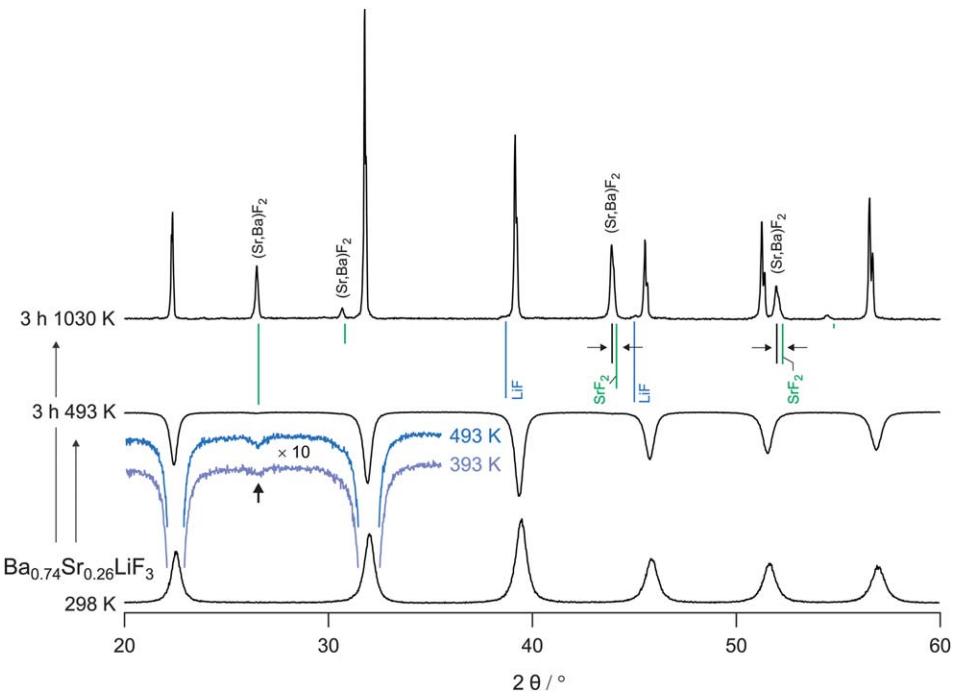

Fig. 11 XRPD pattern of mechanosynthesized $Ba_{0.74}Sr_{0.26}LiF_3$ which was annealed for 3 h at the temperatures indicated. Decomposition of the sample starts when it is exposed to 393 K. The new XRPD peaks emerging (see pattern at the top) can be attributed to a mixed (Sr,Ba)F_2 phase because the peaks at large diffraction angles, in particular, shift towards lower 2θ values. This indicates lattice expansion due to the incorporation of larger Ba^{2+} cations into the cubic structure of SrF_2. Narrowing of the XRPD peaks results from grain growth of the initially nm-sized crystallites. The same features were observed by *in situ* X-ray diffraction (see Fig. S1, ESI†).

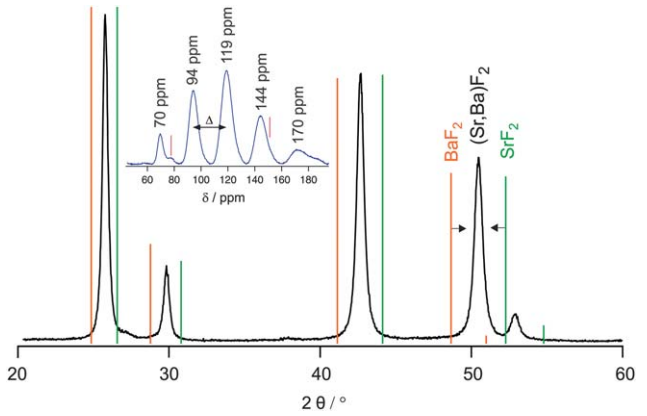

Fig. 12 XRPD pattern of $(Sr,Ba)F_2$ which was prepared by ball milling of SrF_2 with an equimolar amount of BaF_2 in a planetary mill for 3 h at 600 rpm. Whereas the XRPD peaks of SrF_2 shift towards smaller angles, those attributed to BaF_2 appear at larger 2θ values which clearly indicates the formation of a new phase with mixed cations. Inset: Corresponding ^{19}F MAS NMR spectrum recorded at a spinning speed of 60 kHz and a resonance frequency of 471 MHz. The five nearly equidistant NMR signals ($\Delta \approx 25$ ppm) represent the different cation environments the F ions are exposed to in the structurally disordered mixed phase. Vertical lines in the inset point to NMR intensities of residual SrF_2 and BaF_2, respectively.

amounts of Sr cannot be incorporated into $BaLiF_3$ completely. In contrast, if SrF_2 is absent, the formation of $BaLiF_3$ by high-energy ball milling of LiF together with BaF_2 is clearly finished after 3 h.[40]

Let us note that mechanical treatment of SrF_2 with CaF_2 instead of BaF_2 also leads to the formation of $(Ca,Sr)F_2$ solid solutions. See ref. 38 and 23 where the ionic direct current (dc) conductivity of metastable $(Ba,Ca)F_2$ is studied which was prepared by mechanical treatment in a very similar way. Similarly to the situation in $(Ba,Sr)LiF_3$, in mixed $(Sr,Ba)F_2$ (as well as in $(Ca,Sr)F_2$ as mentioned above[49]) the NMR chemical shift of fluorine depends on the number of different earth alkali cations in the (direct) neighbourhood of the nuclei. The inset of Fig. 12 shows the ^{19}F MAS NMR spectrum of mechanosynthesized $(Sr,Ba)F_2$. Despite the structural disorder of the nanocrystalline material different NMR signals are clearly resolved. The main signals are labeled by their chemical shift values. Vertical lines indicate the position of the NMR signals of the source materials SrF_2 (78(1) ppm) and cubic BaF_2 (152(1) ppm), respectively. Most probably, the NMR lines showing up at about 94, 119, and 144 ppm represent the mixed configurations $[Sr]_3[Ba]$, $[Sr]_2[Ba]_2$, and $[Sr][Ba]_3$, respectively. Expectedly, the signal attributed to $[Sr]_2[Ba]_2$ shows the highest intensity. Interestingly, the NMR signals show up in an almost equidistant manner; beginning from about 70 ppm the ^{19}F NMR chemical shift continuously increases in steps of 25 ppm. This is very similar to the situation in $(Ca,Sr)F_2$.[49] The NMR signal attributed to F in the neighbourhood of a $[Sr]_2[Ba]_2$ configuration appears at $(\delta_{iso}(SrF_2) + \delta_{iso}(BaF_2))/2$. In agreement with Vegard's law the lattice constant a of $Sr_{0.5}Ba_{0.5}F_2$ turns out to be 0.60 nm. This is exactly the average of the lattice constants a of the two source materials, BaF_2 (0.62 nm) and SrF_2 (0.58 nm).

The decomposition of $(Ba,Sr)LiF_3$ can also be followed by ^{19}F MAS NMR. In Fig. 13 NMR spectra of $Ba_{0.74}Sr_{0.26}LiF_3$ (see Fig. 5) which was heated for 3 h at 393 K and 493 K, respectively, are shown. Note that the NMR spectra were recorded on the same samples after they were kept under air atmosphere for several weeks. They clearly show the re-formation of the binary fluorides LiF, SrF_2 and cubic BaF_2 which can be unambiguously identified by their specific ^{19}F NMR chemical shifts (Fig. 13b). Interestingly, as also verified by XRPD patterns, which are not shown here for brevity, the long-term exposition of the material to air does not lead to the formation of any detectable oxides or oxofluorides although this might be expected in the case of nanocrystalline materials characterised by an extremely large surface area. As indicated by TEM

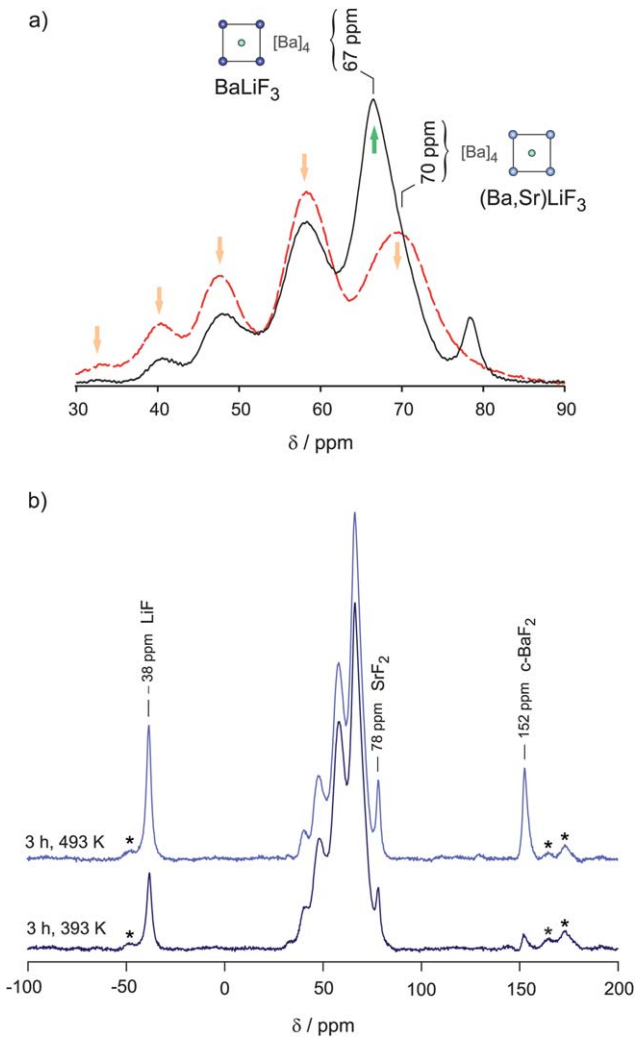

Fig. 13 ^{19}F MAS NMR spectra of $Ba_{1-x}Sr_xLiF_3$ with $x = 0.26$ which was annealed at the temperatures indicated (see text for further details). Data were recorded at a spinning speed of 60 kHz and a resonance frequency of 471 MHz. (a) Comparison of the NMR spectrum of the sample annealed at 493 K with that of the as prepared one (see Fig. 5). The signal at about 67 ppm reflects F in $BaLiF_3$ which is re-formed. The intensity at approximately 78 ppm is due to SrF_2 which is almost free of any Ba. (b) NMR spectra showing the re-formation of LiF and cubic BaF_2. Any significant amount of orthorhombic BaF_2 cannot be detected. The shallow NMR signal at about 130 ppm shows a very small amount of mixed $(Ba,Sr)F_2$.

micrographs (see above), the surface of the nm-sized crystallites partly reveals structural disorder. Thus, it is expected to be highly reactive. However, it becomes evident from Fig. 13b that (Ba,Sr)LiF_3, in contrast to its behaviour at high temperature, decomposes in such a way that also BaF_2 is re-formed. In agreement with the NMR results the corresponding XRPD pattern reveals the formation of cubic BaF_2. Most probably, the (Ba,Sr)LiF_3 left after heat treatment, which is largely depleted or almost free of Sr (see the following paragraph), might be much more sensitive to moisture than a sample directly prepared from the binary fluorides.

The reappearance of the NMR signals of the binary fluorides at −38(1), 78(1) and 152(1) ppm, respectively, is accompanied by a decrease of those lines which are attributed to (Ba,Sr)LiF_3 (Fig. 13a). In accordance with the conclusion drawn from the XRPD measurements, the signal at 66(1) ppm unequivocally shows that $BaLiF_3$ almost free of Sr is (partly) re-formed while the signal at about 70 ppm is attributed to an F environment characterised by $[Ba]_4$ in mixed (Ba,Sr)LiF_3 (see Fig. 13a). Orthorhombic BaF_2 does not seem to belong to the main decomposition products observed after exposing the sample to air.

Let us mention that our attempts to prepare phase-pure $Ba_{1-x}Sr_xLiF_3$ with Sr contents of $x = 0.3$ by solid state reaction failed. A mixture of well ground source materials and a mechanosynthesized (Ba,Sr)LiF_3 sample were both heated at 973 K for several hours and then rapidly quenched to room temperature. The corresponding XRPDs (see Fig. S2, ESI†) clearly show the presence of $BaLiF_3$ and SrF_2 as well as a small amount of Sr-rich (Ba,Sr)F_2. The amount of Sr successfully incorporated into $BaLiF_3$ turns out to be approximately 10% at most.

C. Ion transport properties

Ion transport parameters for various freshly prepared samples of $Ba_{1-x}Sr_xLiF_3$ were studied by impedance spectroscopy.[56] Exemplarily, in Fig. 14 the impedance spectra, *i. e.*, the real part of the complex conductivity σ' *versus* frequency ν, of $Ba_{1-x}Sr_xLiF_3$ with $x = 0.26$ are shown. The isotherms are typically composed of a well-defined dc-plateau and a dispersive region showing up at low temperatures and high frequencies.[57] Dc-conductivity values σ_{dc} are obtained by extrapolating the real part σ' of the complex conductivity to $\nu \rightarrow 0$. In our case this is possible for temperatures higher than room temperature. At lower T the dispersive part of $\sigma'(\nu)$ dominates the spectra. Note that electrode polarization effects show up at higher T affecting the impedance data at low frequencies. These blocking effects have to be taken into account when σ_{dc} is read out from the impedance spectra. Alternatively, complex plane representations can be analyzed to obtain conductivity data. In the present case this yields the same results.

The isotherms shown in Fig. 14 represent those of a second run of measurements. After drying the sample, which was prepared in air, for 24 h at 333 K under vacuum, the first impedance spectrum was recorded at 323 K. Measurements were strictly carried out in nitrogen atmosphere. For the first run, the temperature was decreased to 233 K and then increased up to 473 K in steps of 20 K. Immediately after that, a second run of measurements was started for which the temperature was at first

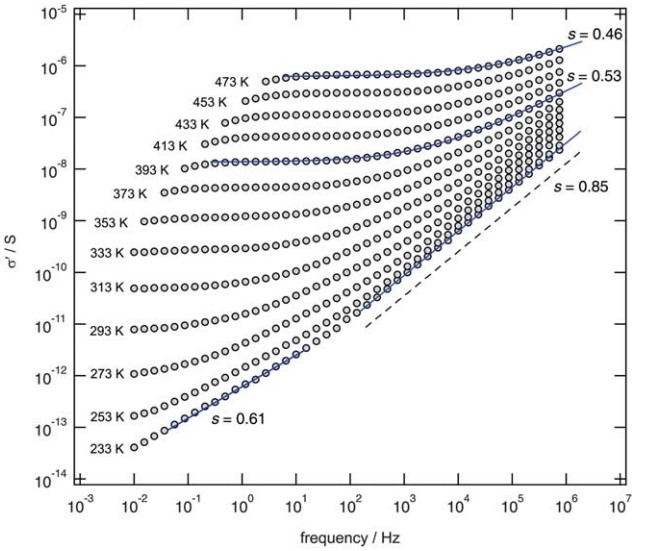

Fig. 14 Conductivity σ' of mechanosynthesized $Ba_{0.74}Sr_{0.26}LiF_3$ plotted double-logarithmically *versus* the measuring frequency. At elevated temperatures the impedance spectra are each composed of a dc-plateau and a dispersive region. At low frequencies and high temperatures distortions show up which are due to space charges accumulating near the blocking Au electrodes leading to a spurious decrease of σ'. A $\sigma' \propto \nu$ frequency dependence would represent constant loss behaviour. The spectrum recorded at the lowest temperature (233 K) is still affected by both dc and ac conductivities. The values indicated represent exponents s of a power law fit using $\sigma' = \sigma_{dc} + A_0\nu^s$.

decreased from 473 K back to 233 K and after that increased once again to 473 K in steps of 20 K. In each case the sample was kept at 473 K for less than 10 min in order to prevent substantial decomposition during heating. The whole procedure is illustrated in Fig. 15, where the dc-conductivity values are plotted as $\sigma_{dc}T$ *versus* the inverse temperature. Obviously, whereas the data of the first run are still affected by traces of water that might be absorbed during the synthesis process, the σ_{dc} values of the second run reflect the ionic conductivity of (Ba,Sr)LiF_3. This is corroborated by the observation that σ_{dc} values recorded at temperatures up to 550 K with the HP impedance analyzer fit to the data sampled at lower temperature utilizing the Novocontrol system. Thus, any further changes of σ_{dc} do not occur. Certainly, exposing the sample to higher temperatures for much longer times causes the beginning of decomposition as described above.

The data of the second run of measurements follow Arrhenius behaviour and yield an activation energy of about 0.76 eV. This value is very similar to that observed for mechanosynthesized, nanocrystalline $BaLiF_3$, recently.[40] Interestingly, the initial impedance spectra of the first run lead to conductivity values which show the same activation energy. The difference of the absolute conductivity values is about one order of magnitude. If this relatively small enhancement is not caused by traces of water as proposed above, it might also be explained by a structural effect. A higher density of defects due to increased structural disorder would cause an enhancement of the pre-exponential factor of the corresponding Arrhenius law for σ_{dc}. The pre-factor depends on the number of available charge carriers as well as an entropy term reflecting the degree of disorder. In a non-annealed mechanosynthesized sample the ion conductivity might be

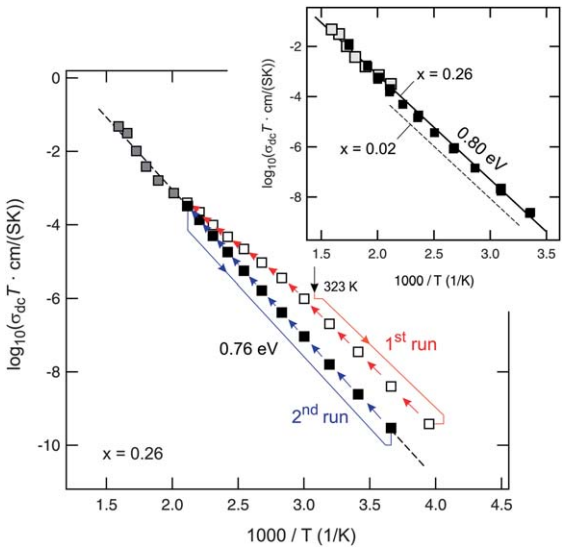

Fig. 15 Arrhenius plot for the dc conductivity ($\sigma_{dc}T$) of mechanosynthesized $Ba_{1-x}Sr_xLiF_3$ with $x = 0.26$ obtained by extrapolating σ' to $\nu \rightarrow 0$ (see Fig. 14). Uncertainties are within the size of the symbols. The dashed line is calculated using an Arrhenius law for $\sigma'_{dc}T$ with an activation energy E_a of about 0.76 eV. The arrows illustrate the chronological order of the measurements. The data of the first (□) and second (■) runs of measurements are obtained with the Novocontrol setup; the other data points (grey-filled squares) are measured by using an HP analyzer (see section II). The latter are also included in the inset and compared with those which were obtained on a $Ba_{0.74}Sr_{0.26}LiF_3$ sample prepared under argon atmosphere. See text for further details. The dashed line shown in the inset represents $\sigma_{dc}T$ of a sample with $x = 0.02$.

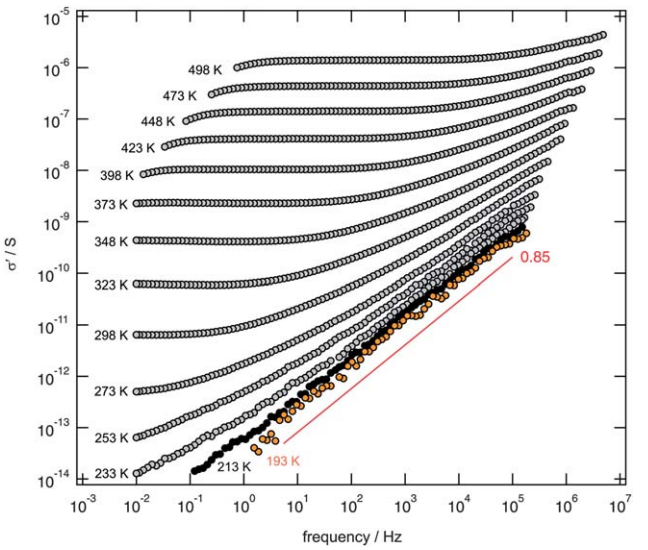

Fig. 16 Impedance spectra of $Ba_{0.74}Sr_{0.26}LiF_3$ which was mechanosynthesized in Ar atmosphere. At very low temperatures the real part of the complex conductivity follows $\sigma' = \nu^{0.85}$ (solid line) when frequencies ranging from 10^0 to 10^5 Hz are regarded. The spectra are very similar to those shown in Fig. 14. However, changes at very low temperatures and high frequencies might be attributed to localized structural relaxation occurring during annealing the sample at 500 K for about 40 min.

controlled by these frozen-in structural features. Annealing at elevated temperatures might cause structural relaxation and thus a slight decrease of σ_{dc}.

In order to enlighten the influence of the preparation atmosphere on ionic conductivity we have examined a sample which was mechanosynthesized and handled in inert gas atmosphere (Fig. 15 and 16). The inset of Fig. 15 shows σ_{dc} values of a sample with the same composition as that in the main figure but which was prepared in Ar atmosphere instead of milling the binary fluorides in air. Prior to the electrical measurements the sample was additionally dried at 500 K for about 40 min under nitrogen atmosphere inside the sample cell. Subsequently, impedance spectra were recorded in steps of 25 K down to 193 K. The corresponding isotherms are shown in Fig. 16. A second run including an initial drying period of 30 min at 573 K does not lead to any further changes of σ_{dc}. Conductivity values were readily reproduced through subsequent heating and cooling cycles. For comparison, in the inset of Fig. 15 also the high-temperature conductivity values of the sample prepared in air are included.

The solid lines shown in Fig. 14 represent fits according to a simple power law:[58] $\sigma' = \sigma_{dc} + A_0\nu^s$ with A_0 being the dispersion parameter. The exponent s usually ranges from 0 to 1. $s = 0$ is expected for uncorrelated motion of the ions which is usually expected for ionic conductors with a very low concentration of mobile charge carriers. $s = 1$ represents the so-called nearly constant loss (NCL)[57] being often observed at low temperatures. There are many studies which show that the NCL might be ascribed to caged, *i.e.*, highly localized dynamics which does not contribute to long-range transport.[57] However, a clear understanding of this phenomenon is still missing. It can be seen from Fig. 14 that the impedance spectrum recorded at 233 K can be divided into two regions obeying different power laws. At low frequencies the σ' values are influenced by both dc and ac conductivities. The slight dependence of s on temperature (see the values given in Fig. 14) vanishes after annealing the sample softly at higher T. For comparison, see the impedance spectra shown in Fig. 16 of the sample prepared in Ar atmosphere. As mentioned above this sample was exposed to 573 K yielding conductivity isotherms being similar in shape in the high frequency regime. Recently, similar observations were made for mechanosynthesized $BaLiF_3$ and ascribed to thermally-induced structural relaxation processes affecting the transport characteristics on short length scales only.[40]

For the sake of completeness, the dotted line of the inset of Fig. 15 marks the conductivity values of a sample with $x = 0.02$. The ion transport characteristics of $(Ba_{0.98}Sr_{0.02})LiF_3$ are very similar to those observed for the sample with $x = 0.26$. Careful inspection of the conductivity data shows that starting from $x = 0$ the ion conductivity first decreases by about a factor of about five. Increasing x to 0.12 leads to a small increase of σ_{dc} until the ionic conductivity reaches the σ_{dc} values of pure $BaLiF_3$ whose ionic dc conductivity almost coincides with that of a sample with $x = 0.26$. Thus, varying x in the range from $x = 0$ to $x = 0.26$ does not exhibit a great influence of the Ba:Sr ratio on the conductivity of the inverse perovskites studied.

D. Conclusions and outlook

$(Ba,Sr)LiF_3$ turns out to be a highly metastable quaternary fluoride crystallizing with the inverse perovskite structure. It can

be prepared in high purity by taking advantage of room-temperature high-energy ball milling being a soft synthesis route avoiding high synthesis temperatures. A quasi *in situ* characterization of the mechanosynthesis of (Ba,Sr)LiF_3 is possible since the reaction can abruptly be stopped by switching off the mill. ^{19}F MAS NMR spectroscopy was used to elucidate both the formation mechanisms including possible side reactions as well as decomposition processes clearly starting when the material is exposed to elevated temperatures for many hours. The latter was verified by *ex* as well as *in situ* XRPD measurements. Despite the structural disorder of the material five magnetically inequivalent fluorine sites can be well resolved with the help of ultrafast ^{19}F MAS NMR. The technique helps to understand the mechanically driven solid state reactions from an atomic-scale point of view. NMR spectra reveal the structural changes with both increasing Sr content as well as milling time, *i.e.*, with increasing progress of the reaction. Obviously, $BaLiF_3$ is initially formed into which Sr is increasingly incorporated during milling. The relatively high ionic conductivity of the metastable perovskites studied so far might be further improved by replacement of Ba with other di- as well as trivalent cations using convenient one-step mechanochemical preparation techniques.

Acknowledgements

We thank the workgroup of Prof. Caro (Hannover) for access to the X-ray diffractometers as well as the Edwards evaporator and Prof. Freude (Leipzig) for recording the ^6Li MAS NMR spectrum. Financial support by the Deutsche Forschungsgemeinschaft (DFG) within the frame of the Priority Program SPP 1415 is highly acknowledged. M.W. acknowledges a research grant of the Leibniz University Hannover within in the project DYNAMA (Wege in die Forschung II).

References

1 H. L. Tuller, in *Springer Handbook of Electronic and Photonic Materials*, ed. S. Kasap and P. Capper, Springer, Berlin, 2006, ch. 11, *Ionic Conduction and Applications*, pp. 213–228.
2 E. Kendrick and P. Slater, *Annu. Rep. Prog. Chem., Sect. A*, 2010, **106**, 429.
3 P. Knauth, *Solid State Ionics*, 2009, **180**, 911.
4 A. V. Chadwick, *Phys. Status Solidi A*, 2007, **204**, 631.
5 C. S. Sunandana and P. S. Kumar, *Bull. Mater. Sci.*, 2004, **27**, 1.
6 L. Malavasi, C. A. J. Fisher and M. S. Islam, *Chem. Soc. Rev.*, 2010, **39**, 4370.
7 P. Knauth and J. Schoonman, *Nanocomposites – Ionic Conducting Materials and Structural Spectroscopies*, Springer, New York, 2007.
8 P. G. Bruce, B. Scrosati and J.-M. Tarascon, *Angew. Chem., Int. Ed.*, 2008, **47**, 2930.
9 T. Brezesinski, J. Wang, S. H. Tolbert and B. Dunn, *Nat. Mater.*, 2010, **9**, 146.
10 S. Hull, *Rep. Prog. Phys.*, 2004, **67**, 1233.
11 A. S. Aricó, P. G. Bruce, B. Scrosati, J.-M. Tarascon and W. V. Schalkwijk, *Nat. Mater.*, 2005, **4**, 366.
12 M. Whittingham, *Chem. Rev.*, 2004, **104**, 4271.
13 P. Knauth and H. Tuller, *J. Am. Ceram. Soc.*, 2004, **85**, 1654.
14 J. Maier, *Nat. Mater.*, 2005, **4**, 805.
15 J. Garcia-Barriocanal, A. Rivera-Calzada, M. Varela, Z. Sefrioui, M. R. Diaz-Guillen, K. J. Moreno, J. A. Diaz-Guillen, E. Iborra, A. F. Fuentes and S. J. Pennycook, *et al.*, *ChemPhysChem*, 2009, **10**, 1003.
16 P. Heitjans and M. Wilkening, *MRS Bull.*, 2009, **34**, 915.
17 M. Wilkening, V. Epp, A. Feldhoff and P. Heitjans, *J. Phys. Chem. C*, 2008, **112**, 9291.
18 P. Heitjans, S. Indris, and M. Wilkening, in *Nanocomposites – Ionic Conducting Materials and Structural Spectroscopies*, edited by P. Knauth and J. Schoonman, Springer, New York, 2007, p. 227.
19 P. Heitjans, M. Masoud, A. Feldhoff and M. Wilkening, *Faraday Discuss.*, 2007, **134**, 67.
20 P. Heitjans and S. Indris, *J. Phys.: Condens. Matter*, 2003, **15**, R1257.
21 M. Wilkening, S. Indris and P. Heitjans, *Phys. Chem. Chem. Phys.*, 2003, **5**, 2225.
22 N. Sata, K. Ebermann, K. Eberl and J. Maier, *Nature*, 2000, **408**, 946.
23 B. Ruprecht, M. Wilkening, A. Feldhoff, S. Steuernagel and P. Heitjans, *Phys. Chem. Chem. Phys.*, 2009, **11**, 3071.
24 A. F. Fuentes, K. J. Moreno, J. Santamaría, C. Léon, and U. Amador, in Solid-State Ionics-2006, edited by T. R. Armstrong and C. Masquelier and Y. Sadaoka, 2007, vol. 972 of *Mater. Res. Soc. Symp. Proc.*, p. 97.
25 K. J. Moreno, A. F. Fuentes, M. Maczka, J. Hanuza, U. Amador, J. Santamaría, and C. Léon, *Phys. Rev. B*75 (2007).
26 M. Jansen, K. Doll and J. C. Schön, *Acta Crystallogr., Sect. A: Found. Crystallogr.*, 2010, **66**, 518.
27 C. Mellot-Draznieks, S. Girard, G. Férey, J. C. Schön, Z. Čančarević and M. Jansen, *Chem.–Eur. J.*, 2002, **8**, 4103.
28 M. Wevers, J. Schön and M. Jansen, *J. Phys.: Condens. Matter*, 1999, **11**, 6487.
29 G. Golubkova, E. Belyaev and O. Lomovsky, *J. Alloys Compd.*, 1998, **270**, 224.
30 V. Šepelák, I. Bergmann, A. Diekmann, P. Heitjans and K. D. Becker, *Rev. Adv. Mater. Sci.*, 2008, **18**, 349.
31 V. Šepelák, S. Indris, I. Bergmann, A. Feldhoff, K. D. Becker and P. Heitjans, *Solid State Ionics*, 2006, **177**, 2487.
32 M. Nagumo, T. Suzuki, and K. Tsuchida, in Metastable, mechanically alloyed and nanocrystalline materials, edited by R. Schulz, 1996, vol. 225 of *Mater. Sci. Forum*, p. 581.
33 V. Šepelák, K. D. Becker, I. Bergmann, S. Suzuki, S. Indris, A. Feldhoff, P. Heitjans and C. P. Grey, *Chem. Mater.*, 2009, **21**, 2518.
34 V. Šepelák, I. Bergmann, A. Feldhoff, P. Heitjans, F. Krumeich, D. Menzel, F. J. Litterst, S. J. Campbell and K. D. Becker, *J. Phys. Chem. C*, 2007, **111**, 5026.
35 V. Šepelák, A. Feldhoff, P. Heitjans, F. Krumeich, D. Menzel, F. Litterst, I. Bergmann and K. Becker, *Chem. Mater.*, 2006, **18**, 3057.
36 V. V. Boldyrev, *Russ. Chem. Rev.*, 2006, **75**, 177.
37 E. Avvakumov, M. Senna, and N. Kosova, *Soft Mechanochemical Synthesis: A Basis for New Chemical Technologies*, Kluwer Academic Publishers, Boston, 2001.
38 B. Ruprecht, M. Wilkening, S. Steuernagel and P. Heitjans, *J. Mater. Chem.*, 2008, **18**, 5412.
39 A. Boumriche, J. Y. Gesland, A. Bulou, M. Rousseau, J. L. Fourquet and B. Hennion, *Solid State Commun.*, 1994, **91**, 125.
40 A. Düvel, M. Wilkening, R. Uecker, S. Wegner, V. Šepelák and P. Heitjans, *Phys. Chem. Chem. Phys.*, 2010, **12**, 11251.
41 H. Swanson, H. McMurdie, M. Morris and E. Evans, *Natl. Bur. Stand. (U.S.), Monogr*, 1967, **25**, 35.
42 V. Goldschmidt, *Skr. Norske Vidensk.-Akad. (Math.-Naturw. Kl.)*, 1926, **2**.
43 R. El Ouenzerfi, S. Ono, A. Quema, M. Goto, N. Sarukura, T. Nishimatsu, N. Terakubo, H. Mizuseki, Y. Kawazoe, A. Yoshikawa, *et al.*, *Jpn. J. Appl. Phys.* 43, L 1140 (2004).
44 P. Scherrer, *Göttinger Nachrichten*, 1918, **2**, 98.
45 G. K. Williamson and W. H. Hall, *Acta Metall.*, 1953, **1**, 22.
46 G. Chin, M. Green, L. van Uitert and W. Hargreaves, *J. Mater. Sci.*, 1973, **8**, 1421.
47 A. Düvel, M. Wilkening, S. Wegner, A. Feldhoff, V. Šepelák and P. Heitjans, *Solid State Ionics*, 2011, **184**, 65.
48 A. Picinin, R. R. Deshpande, A. S. S. de Camargo, J. P. Donoso, J. P. Rino, H. Eckert and M. A. P. Silva, *J. Chem. Phys.*, 2008, **128**, 224705.
49 R. E. Youngman and C. M. Smith, *Phys. Rev. B: Condens. Matter Mater. Phys.*, 2008, **78**, 014112.
50 B. Bureau, G. Silly, J. Buzaré and J. Emery, *Chem. Phys.*, 1999, **249**, 89.
51 M. Body, G. Silly, C. Legein and J. Buzaré, *Inorg. Chem.*, 2004, **43**, 2474.
52 A. Zheng, S.-B. Liu and F. Deng, *J. Phys. Chem. C*, 2009, **113**, 15018.

53 S. Dorfman, F. Jiang, Z. Mao, A. Kubo, Y. Meng, V. Prakapenka and S. Duffy, *Phys. Rev. B: Condens. Matter Mater. Phys.*, 2010, **81**, 174121.
54 J. M. Leger, J. Haines, A. Atouf, O. Schulte and S. Hull, *Phys. Rev. B: Condens. Matter*, 1995, **52**, 13247.
55 V. Kanchana, G. Vaitheeswaran and M. Rajagopalan, *J. Alloys Compd.*, 2003, **359**, 66.
56 E. Barsoukov and J. R. MacDonald, *Impedance Spectroscopy – Theory, Experiment and Applications*, Wiley & Sons Hoboken, New Jersey, 2005.
57 K. Funke, C. Cramer, and D. Wilmer, in *Diffusion in Condensed Matter – Methods, Materials, Models*, ed. P. Heitjans and J. Kärger, Springer, Berlin, 2005, chap. 9, pp. 857–893.
58 A. Jonscher, *Nature*, 1977, **267**, 673.

